OPEN ACCESS

Original research

Combining ferroptosis induction with MDSC blockade renders primary tumours and metastases in liver sensitive to immune checkpoint blockade

Claire Conche,[1,2] Fabian Finkelmeier ,[1,2,3] Marina Pešić,[1,2] Adele M Nicolas,[1,2] Tim W Böttger,[1,2] Kilian B Kennel,[1,2] Dominic Denk,[1,2,3] Fatih Ceteci,[1,2] Kathleen Mohs,[1,2] Esther Engel,[1,2] Özge Canli,[1] Yasamin Dabiri,[1,2] Kai-Henrik Peiffer ,[3] Stefan Zeuzem,[3] Gabriela Salinas,[4] Thomas Longerich ,[5] Huan Yang,[6] Florian R Greten [1,2,7]

► Additional supplemental material is published online only. To view, please visit the journal online (http://dx.doi.org/10.1136/gutjnl-2022-327909).

For numbered affiliations see end of article.

Correspondence to
Professor Florian R Greten, Institute for Tumor Biology and Experimental Therapy, Frankfurt/Main 60596, Germany; greten@gsh.uni-frankfurt.de

CC and FF contributed equally.

CC and FF are joint first authors.

Received 21 May 2022
Accepted 7 January 2023
Published Online First 27 January 2023

ABSTRACT

Objective Investigating the effect of ferroptosis in the tumour microenvironment to identify combinatory therapy for liver cancer treatment.

Design Glutathione peroxidase 4 (GPx4), which is considered the master regulator of ferroptosis, was genetically altered in murine models for hepatocellular carcinoma (HCC) and colorectal cancer (CRC) to analyse the effect of ferroptosis on tumour cells and the immune tumour microenvironment. The findings served as foundation for the identification of additional targets for combine therapy with ferroptotic inducer in the treatment of HCC and liver metastasis.

Results Surprisingly, hepatocyte-restricted GPx4 loss does not suppress hepatocellular tumourigenesis. Instead, GPx4-associated ferroptotic hepatocyte death causes a tumour suppressive immune response characterised by a CXCL10-dependent infiltration of cytotoxic $CD8^+$ T cells that is counterbalanced by PD-L1 upregulation on tumour cells as well as by a marked HMGB1-mediated myeloid derived suppressor cell (MDSC) infiltration. Blocking PD-1 or HMGB1 unleashes T cell activation and prolongs survival of mice with *Gpx4*-deficient liver tumours. A triple combination of the ferroptosis inducing natural compound withaferin A, the CXCR2 inhibitor SB225002 and α-PD-1 greatly improves survival of wild-type mice with liver tumours. In contrast, the same combination does not affect tumour growth of subcutaneously grown CRC organoids, while it decreases their metastatic growth in liver.

Conclusion Our data highlight a context-specific ferroptosis-induced immune response that could be therapeutically exploited for the treatment of primary liver tumours and liver metastases.

WHAT IS ALREADY KNOWN ON THIS TOPIC

⇒ Glutathione peroxidase 4 has been suggested to confer tumour suppressive functions in a cell autonomous manner.
⇒ $CD8^+$ T cells can induce ferroptosis in tumour cells.

WHAT THIS STUDY ADDS

⇒ In hepatocellular carcinoma (HCC), ferroptosis does not provide a cell autonomous tumour suppressor function, but rather triggers an adaptive immune response placing ferroptosis upstream of $CD8^+$ T cells.
⇒ T cell infiltration by cCAS/STING-dependent CXCL10 secretion is associated with IFNγ secretion by $CD8^+$ T cells, ultimately resulting in PD-L1 upregulation on tumour cells.
⇒ On the contrary, ferroptosis triggers tumour infiltration of myeloid derived suppressor cells (MDSCs) via HMGB1 in HCC but not in colorectal cancer (CRC).
⇒ Ferroptosis is as potent anticancer target for the treatment of HCC and CRC liver metastasis in combination with immune checkpoint and MDSC blockade while primary CRC is resistant to this combinatorial treatment.

HOW THIS STUDY MIGHT AFFECT RESEARCH, PRACTICE OR POLICY

⇒ Provide a novel therapeutic option for the treatment HCC and CRC liver metastasis.
⇒ The withaferin A (WFA), α-PD-1 and SB225002 combinatory treatment could potentially extend to liver metastases from other tumour types considering that its efficacy on liver metastasis is independent on the primary tumour response and that ferroptosis is a non-targeted antitumour approach.

Linked

► http://dx.doi.org/10.1136/gutjnl-2023-329472

Check for updates

To cite: Conche C, Finkelmeier F, Pešić M, *et al*. *Gut* 2023;**72**:1774–1782.

INTRODUCTION

Ferroptosis is a non-apoptotic iron-dependent type of cell death that depends on the accumulation of lipid peroxides that cause disruption of cell membranes.[1 2] Ferroptosis differs from other types of cell death by cellular morphology and the responsible signalling pathways as it cannot be rescued by caspase-associated, receptor-associated adaptor kinase (RIP) and tumour necrosis factor α (TNFα) inhibition while it is sensitive to reducing and iron chelating agents.[3] Although the terminal executive molecular mechanisms of ferroptosis are yet to be clearly identified the initials signals regulating lipid peroxidation are well documented. Physiologically, ferroptosis is prevented by the

selenoenzyme glutathione peroxidase 4 (GPx4) which comprises an important constituent of the cellular antioxidant network.[4] GPx4 activity depends on glutathione whose concentration relies on cysteine import by the System Xc^-. Not surprisingly lipoxygenase (ALOX), polyunsaturated fatty acids, which are sensitive to lipid peroxidation acetyl-CoA enzymes have been shown to be involved in ferroptosis.[5]

Cancer cells tend to be more sensitive to ferroptosis which might be correlated to their oncogenic profiles.[5] Indeed, tumour suppressors p53 and BAP1 regulate the expression of SCL7A11 and thereby the sensitivity of tumour cells to ferroptosis.[6 7] Additionally, p53 has been shown to modulate ferroptosis through alternative pathways including Alox and P21.[8] Retinoblastoma proteins have been reported to correlate with the ferroptotic resistance in hepatocellular carcinoma (HCC).[9] The role of Ras in the regulation of ferroptosis has to be elucidated and might be context dependent with reports of RAS either promoting or limiting ROS and ferroptosis.[10] Ferroptosis can be triggered either by increasing the cellular iron load and ROS generation or by inhibiting the antioxidant machinery. Among ferroptosis targeting pharmacological agents available, Erastin, inhibitor of System Xc^- and RSL3 and withaferin A (WFA) all of which inhibit GPx4 are potent ferroptosis inducers.[11 12] Importantly, sorafenib, which has been used for a long time as a first-line therapy for advanced HCC induces ferroptosis[13] while ferroptosis in non-viral and non-tumour liver diseases tends to aggravate the pathology.[14] Paradox effects of ferroptosis were also reported for pancreatic cancer.[15] Interestingly, there is also a link between ferroptosis and immune cell activation. IFNγ and arachidonic acid releasing $CD8^+$ T cells trigger an ACSL4-dependent ferroptosis.[16 17] Moreover, ferroptosis associated 8-OHdG activates the STING pathway and triggers macrophage infiltration and M2-polarisation thereby promoting pancreatic tumourigenesis.[18 19] Early ferroptotic but not late ferroptotic cells can trigger T cell mediated antitumuor vaccination in a fibrosarcoma murine model[20] raising the possibility that a ferroptosis-dependent cytotoxic antitumourigenic adaptive immune response may be context dependent.

Here, we describe the contribution of hepatocyte ferroptosis to $CD8^+$ T cell activation in a model of primary HCC and metastatic colon cancer and identify the complex interaction between cancer, myeloid and T cells within the liver tumour microenvironment that could offer a new therapeutic approach for the treatment of HCC and liver metastases.

RESULTS

Hepatocyte restricted GPX4 deletion induces ferroptosis and inflammation

To examine GPx4 function in liver, we crossed floxed *Gpx4* mice ($Gpx4^{F/F}$) to albumin-Cre expressing mice to generate $Gpx4^{\Delta/\Delta hep}$ mice. In vivo, *Gpx4* deletion is usually compensated by the high amount of vitamin E typically present in regular chow.[7 21–23] Accordingly, while $Gpx4^{F/F}$ mice were healthy, $Gpx4^{\Delta/\Delta hep}$ mice succumbed to liver failure within 21 days when placed on a vitamin E-depleted diet ($diet^{\Delta vitE}$), which was not observed when mice were kept on a regular chow (online supplemental figure 1A). Gpx4-dependent liver damage was characterised by distinct zonal necrosis accompanied by sinusoidal congestion, haemorrhage and signs of immune cell infiltration (online supplemental figure 1B). In line with ferroptosis induction in vivo, hepatocytes from $Gpx4^{\Delta/\Delta hep}$ mice on $diet^{\Delta vitE}$ were TUNEL positive while caspase-3 negative with increased expression of lipids peroxidation markers MDA and 4-HNE as well of the newly identify ferroptotic marker CD71[24] (online supplemental figure 1B). Induction of ferroptosis was further confirmed in primary $Gpx4^{\Delta/\Delta hep}$ hepatocytes ex vivo that could only survive in the presence of ferroptosis inhibitors (online supplemental figure 1C). RNAseq analysis and *GOterm* pathway analysis of livers from $Gpx4^{F/F}$ and $Gpx4^{\Delta/\Delta hep}$ mice revealed a significant enrichment of genes connected to inflammatory and immune response pathways (online supplemental figure 1D,E) confirming that hepatocyte-specific Gpx4 deletion causes ferroptosis in vitro as well as in vivo leading to acute liver failure and inflammation.

Ferroptosis does not suppress HCC development

Given that many of the gene products upregulated in ferroptotic livers are known to promote tumour development,[25] we reasoned that during tumourigenesis, ferroptosis may counteract the previously suggested cell autonomous tumour suppression[6 7] by creating a proinflammatory, protumourigenic microenvironment. Thus, to examine the consequences of *Gpx4* loss during liver tumourigenesis, we took advantage of a transposon-based mouse model of liver cancer,[21 26] that is achieved by hydrodynamic tail vein injection (HTVI) of a construct encoding for two oncogenes, $Nras^{G12V}$ and *myr*AKT, together with a transposase encoding plasmid (figure 1A). Nras immunostainings confirmed similar efficiency in transposon delivery after 7 days in both genotypes (figure 1B) and led to multifocal HCC 25 days after HTVI that imposed as highly differentiated hepatocellular tumours with trabecular growth pattern, prominent nucleoli and variable fatty changes and ballooning (figure 1C). In some parts regressive and inflammatory changes could be observed. Moreover, Pearl's Prussian blue staining did not indicate any evidence for enhanced iron deposition in the livers of $Gpx4^{F/F}$ or $Gpx4^{\Delta/\Delta hep}$ mice after HTVI (online supplemental figure 2F). Liver tumours in $Gpx4^{\Delta/\Delta hep}$ mice were characterised by a marked increase in the number of TUNEL-positive cells while the number of apoptotic cells determined by cleaved caspase3 did not differ (figure 1D). Additionally, tumours form $Gpx4^{\Delta/\Delta hep}$ mice showed a significant increase of lipid peroxidation, CD71 expression as well as p-H2AX expression which was associated with elevated levels of oxidative DNA damage marker 8-OHdG (figure 1D), supporting the notion that *Gpx4*-deficient tumour cells died from non-apoptotic, lipid peroxidation induced ferroptosis. Remarkably, tumour load, tumour cell proliferation and survival rates of HCC tumour-bearing mice were comparable between $Gpx4^{F/F}$ controls and $Gpx4^{\Delta/\Delta hep}$ mice (figure 1E,F). Thus, induction of ferroptosis in HCC was not sufficient to confer a significant tumour suppression.

Ferroptosis induces $CD8^+$ T cell activation that is counteracted by PD-L1 upregulation on tumour cells

Considering the ferroptosis-associated inflammatory response during liver failure (online supplemental figure 1D,E), we examined gene expression profiles on day 25 of the transposon-induced HCC model and found a similar upregulation of several chemokines and cytokines (figure 2A) indicating that tumour-associated hepatocyte ferroptosis triggered an immune reaction. Immunofluorescence revealed an increased number of $CD3^+$ and $CD8^+$ T cells in $Gpx4^{\Delta/\Delta hep}$ tumours which, however, was accompanied by a marked upregulation of PD-L1 in tumours (figure 2B). PD-L1 upregulation on tumour cells did not correlate with an overall increased T cell exhaustion in $Gpx4^{\Delta/\Delta hep}$ tumours based on a comparable expression of activation and exhaustion markers comparing $CD8^+$ T cells from $Gpx4^{\Delta/\Delta hep}$ and $Gpx4^{F/F}$ tumours

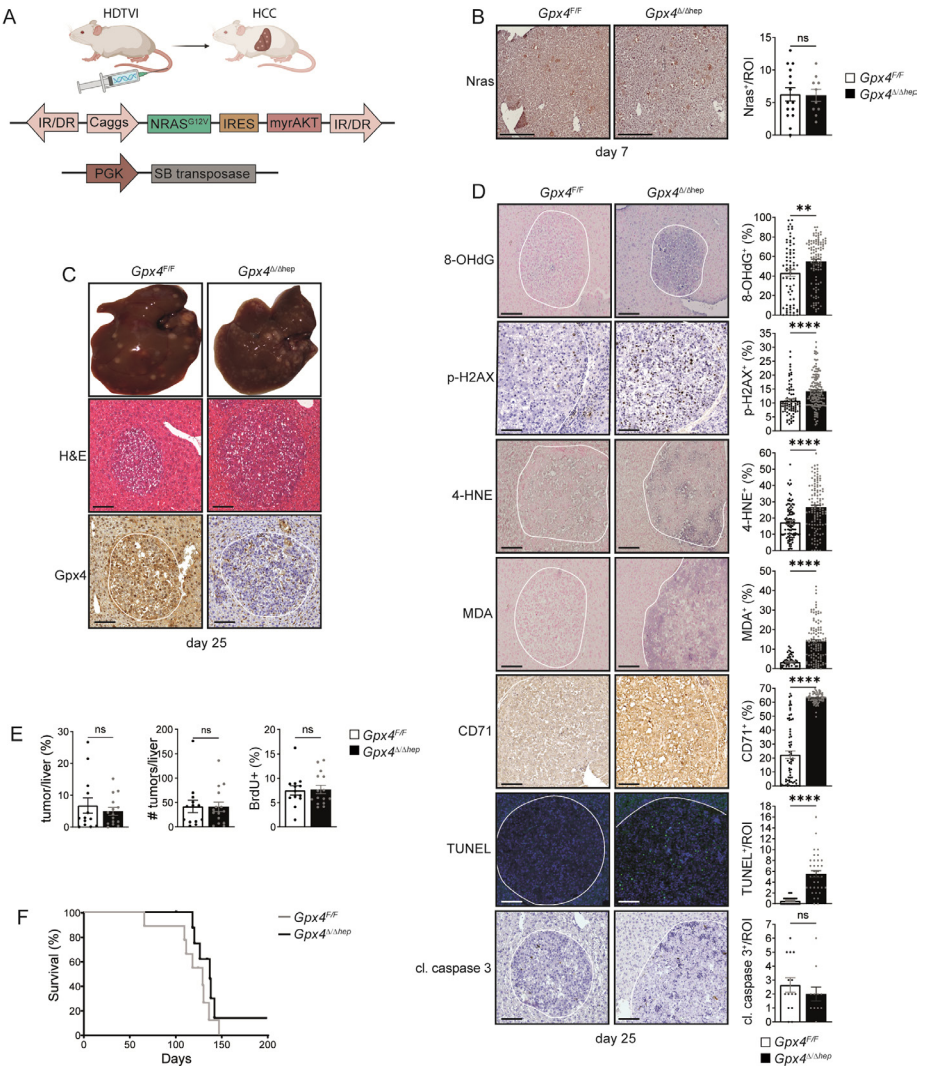

Figure 1 Ferroptotic induction in a murine model of HCC is not sufficient to limit tumour growth. (A) Scheme of HCC murine model with HTVI of oncogenic Nrsas^{G12V} and myristoylated-AKT together with sleeping beauty (SB). (B) Nras immunohistochemical analysis in livers of *Gpx4*$^{F/F}$ and *Gpx4*$^{\Delta/\Delta hep}$ mice 7 days after HTVI (n≥10). (C) Representative images of multifocal HCC and H&E and Gpx4-IHC staining of livers of *Gpx4*$^{F/F}$ and *Gpx4*$^{\Delta/\Delta hep}$ mice 25 days after HTVI. (D) Immunohistochemical analysis of 8-OHdG$^+$ (n≥=73), p-H2AX$^+$ (n≥80), 4-HNE$^+$ (n≥99), MDA$^+$ (n≥59), CD71$^+$ (n≥69), cleaved-caspase 3$^+$ (n≥11) and TUNEL$^+$ (n≥=30) cells in liver tumours of *Gpx4*$^{F/F}$ and *Gpx4*$^{\Delta/\Delta hep}$ mice. (E) Quantification of tumour area percentage to the liver and number of tumours per liver from H&E-stained serial sections. Immunohistochemical analysis of BrdU incorporation in tumours (n≥13). (F) Survival of *Gpx4*$^{F/F}$ and *Gpx4*$^{\Delta/\Delta hep}$ mice after HTVI (n=9), p=0176 by log-rank (Mantel-Cox) test. (A–E) Scale bars=100 µm. Data are mean±SEM, n.s. not significant, **p≤0.01, ****p≤0.0001 by t-test. HCC, hepatocellular carcinoma; HTVI, hydrodynamic tail vein injection; IR/DR, inverted repeats and direct repeats; IRES, internal ribosome entry site.

(online supplemental figure 2A). Instead, CD8$^+$ T cells isolated from *Gpx4*$^{\Delta/\Delta hep}$ ferroptotic tumours had the ability to secrete more IFNγ than CD8$^+$ T cells from control tumours, demonstrating that ferroptosis increased functional activation of the CD8$^+$ T cells (figure 2C). Antibody-mediated CD8$^+$ T cell depletion confirmed that PD-L1 upregulation in tumours was a consequence of enhanced CD8$^+$ T cell infiltration (figure 2D). Next, we aimed to elucidate the link between hepatocyte ferroptosis and CD8$^+$ T cell infiltration. Among the chemokines upregulated in *Gpx4*$^{\Delta/\Delta hep}$ tumours (figure 2A), CXCL10 represents a potent T cell chemoattractant. Freshly isolated primary ferroptotic *Gpx4*$^{\Delta/\Delta hep}$ hepatocytes secreted increased amounts of CXCL10 (figure 2E) confirming that CXCL10 secretion was a direct consequence of ferroptosis. Importantly, deletion of CXCL10 receptor *Cxcr3* prevented CD8$^+$ T cell infiltration into *Gpx4*$^{\Delta/\Delta hep}$ tumours as well as the subsequent CD8$^+$ T cell dependent PD-L1 upregulation (figure 2F,G) underlining the crucial role of hepatocyte-released CXCL10 as a consequence of ferroptosis in driving CD8$^+$ T cell infiltration in *Gpx4*$^{\Delta/\Delta hep}$ tumours. Recently, DNA damage has been associated with induction of CXCL10 as well as other proinflammatory genes,[27] while in pancreatic cancer ferroptosis-induced 8-OHdG formation led to STING activation.[18] Therefore, we examined whether STING blockade would impact CXCL10 secretion. Indeed, CXCL10 release by *Gpx4*$^{\Delta/\Delta hep}$ ferroptotic hepatocytes was sensitive to cGAS/STING inhibitors (figure 2H), consistent with STING dependent macrophage infiltration in pancreatic cancer.[18] Furthermore, we hypothesised that PD-L1 upregulation impaired the ferroptosis-induced T cell antitumour response, which could benefit from α-PD-1 therapy. Consequently, we subjected HCC-bearing mice to immune checkpoint

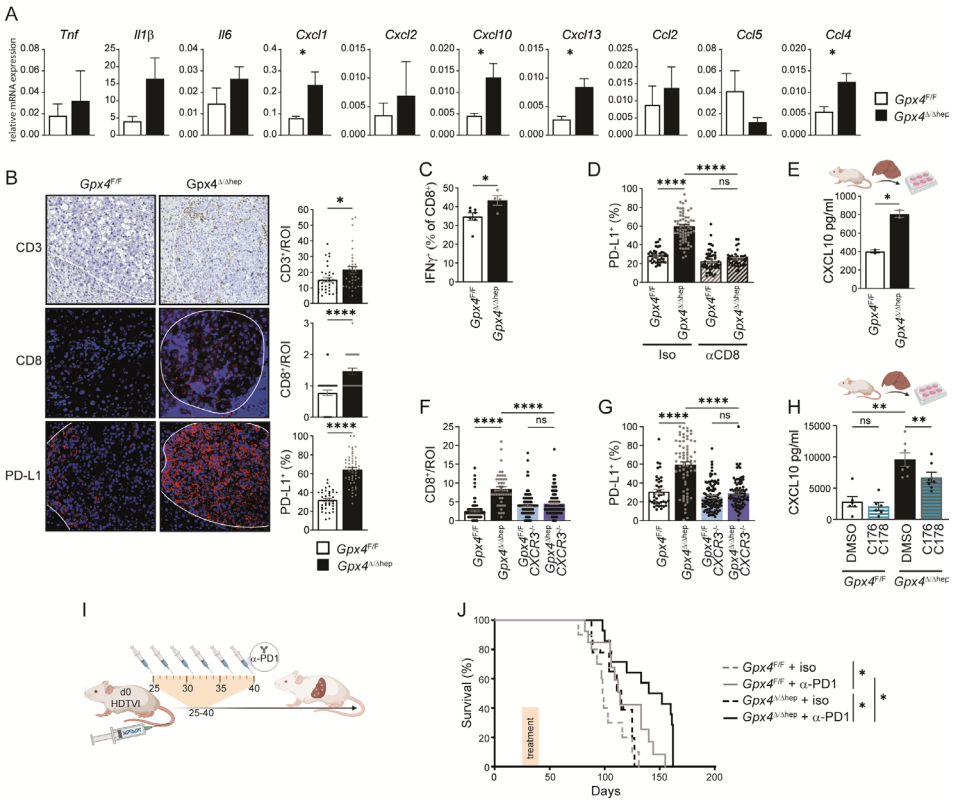

Figure 2 Ferroptosis in HCC induces immune reaction with T cell activation dampened by PD-L1 upregulation. (A) Gene expression quantification by quantitative RT-PCR in tumours from *Gpx4*$^{F/F}$ and *Gpx4*$^{\Delta/\Delta hep}$ mice 25 days after HTVI (n=5). (B) Immunohistochemical analysis of CD3$^+$ (n=35), CD8 (n≥36), PD-L1$^+$ (n=38) cells in HCC tumours of *Gpx4*$^{F/F}$ and *Gpx4*$^{\Delta/\Delta hep}$ mice after HTVI. Scale bars=100 µm. (C) Flow cytometry analysis of IFNγ expression in CD8 T cells from liver of *Gpx4*$^{F/F}$ and *Gpx4*$^{\Delta/\Delta hep}$ tumour bearing mice after PMA/Ionomycin stimulation (n≥4). (D) Immunofluorescence quantification of PD-L1 expression in HCC tumours from *Gpx4*$^{F/F}$ *and Gpx4*$^{\Delta/\Delta hep}$ mice treated with depleting α-CD8 or Rat IgG2b, κ antibodies (n≥42). (E) CXCL10 release by primary hepatocytes from *Gpx4*$^{F/F}$ and *Gpx4*$^{\Delta/\Delta hep}$ mice ex vivo for 4 hours (n=2). (F, G) Immunofluorescence quantification of CD8$^+$ T cells infiltration (F) and PD-L1 expression (G) in HCC tumours from *Gpx4*$^{F/F}$, *Gpx4*$^{\Delta/\Delta hep}$, *Gpx4*$^{F/F}$*CXCR3*$^{-/-}$, *Gpx4*$^{\Delta/\Delta hep}$*CXCR3*$^{-/-}$ mice (n≥40). (H) CXCL10 secretion by *Gpx4*$^{F/F}$ and *Gpx4*$^{\Delta/\Delta hep}$ primary hepatocytes ex vivo treated with 10 µM of C176 and C178 or DMSO for 4 hour (n≥6). (I) Treatment scheme for i.p. injections, of α-PD-1 or isotype (Rat IgG2a,κ). (J) Survival of *Gpx4*$^{F/F}$+ isotype (Rat IgG2a,κ) (n=10), *Gpx4*$^{F/F}$ + α-PD-1 (n=13), *Gpx4*$^{\Delta/\Delta hep}$ + isotype (Rat IgG2a,κ) (n=9) and *Gpx4*$^{\Delta/\Delta hep}$ +α-PD-1 (n=14) mice with HCC tumours. (A–H) Data are mean±SEM, n.s not significant *p≤0.05, **p≤0.01, ****p≤0.0001 by t-test (A–C, E) or one-way ANOVA with Šídák's multiple comparisons test (D, F–H) of the indicated pairs or by log-rank (Mantel-Cox) test (J). ANOVA, analysis of variance; HTVI, hydrodynamic tail vein injection; PMA, phorbol myristate acetate.

blockade and injected α−PD-1 every 3 days for 16 days starting at day 25 (figure 2I) when we detected immune cell infiltration (figure 2A.B). Even though we applied only one cycle of six injections, α-PD-1 treated *Gpx4*$^{\Delta/\Delta hep}$ mice had a significantly increased survival advantage compared with *Gpx4*$^{\Delta/\Delta hep}$ isotype treated mice or to WT mice treated with α-PD-1 (figure 2J). Thus, ferroptosis triggered a tumour suppressive CD8$^+$ T cell response, which was counteracted by a concomitant PD-L1 upregulation that could be unleashed by α−PD-1 treatment.

Ferroptosis induces immunosuppression by stimulating myeloid derived suppressor cell recruitment

In addition to the pronounced CD8$^+$ T cell infiltration, we also observed enhanced F4/80$^+$ and Gr-1$^+$ myeloid cell infiltration into *Gpx4*$^{\Delta/\Delta hep}$ tumours (figure 3A), comprising potentially myeloid derived suppressor cells (MDSCs) and tumour-associated macrophages (TAMs). Flow cytometric analysis was performed to further characterise the myeloid compartment. We found that neither recruitment of TAMs nor recruitment and activation of dendritic cells (DC) was affected by ferroptosis in *Gpx4*$^{\Delta/\Delta hep}$ tumours (online supplemental figure 3A,B), while M-MDSC and PMN-MDSC infiltration was significantly increased in *Gpx4*$^{\Delta/\Delta hep}$ tumours (figure 3B). The immunosuppressive activity of tumour infiltrating MDSC on T cell proliferation was confirmed and we noticed that ferroptosis significantly increased PMN-MDSC immunosuppressive activity (figure 3C). Next, we investigated how ferroptosis triggered MDSC infiltration in *Gpx4*$^{\Delta/\Delta hep}$ tumours. HMGB1 is a potent recruiter of MDSCs[28] and we could indeed confirm that primary *Gpx4*$^{\Delta/\Delta hep}$ hepatocytes undergoing ferroptosis released significantly higher levels of HMGB1 than control hepatocytes (figure 3D). To test whether HMGB1 blockade would prevent MDSC infiltration and stimulate anti-tumour immunity in *Gpx4*$^{\Delta/\Delta hep}$ mice, we either induced HCC in *Gpx4*$^{\Delta/\Delta hep}$/*Rage*$^{-/-}$ compound mutant mice or treated tumour-bearing *Gpx4*$^{\Delta/\Delta hep}$ single mutant mice with HMGB1 neutralising antibody for 2 weeks starting on day 25 (figure 3E,F). While α-HMGB1 antibody treatment shifted the median survival from

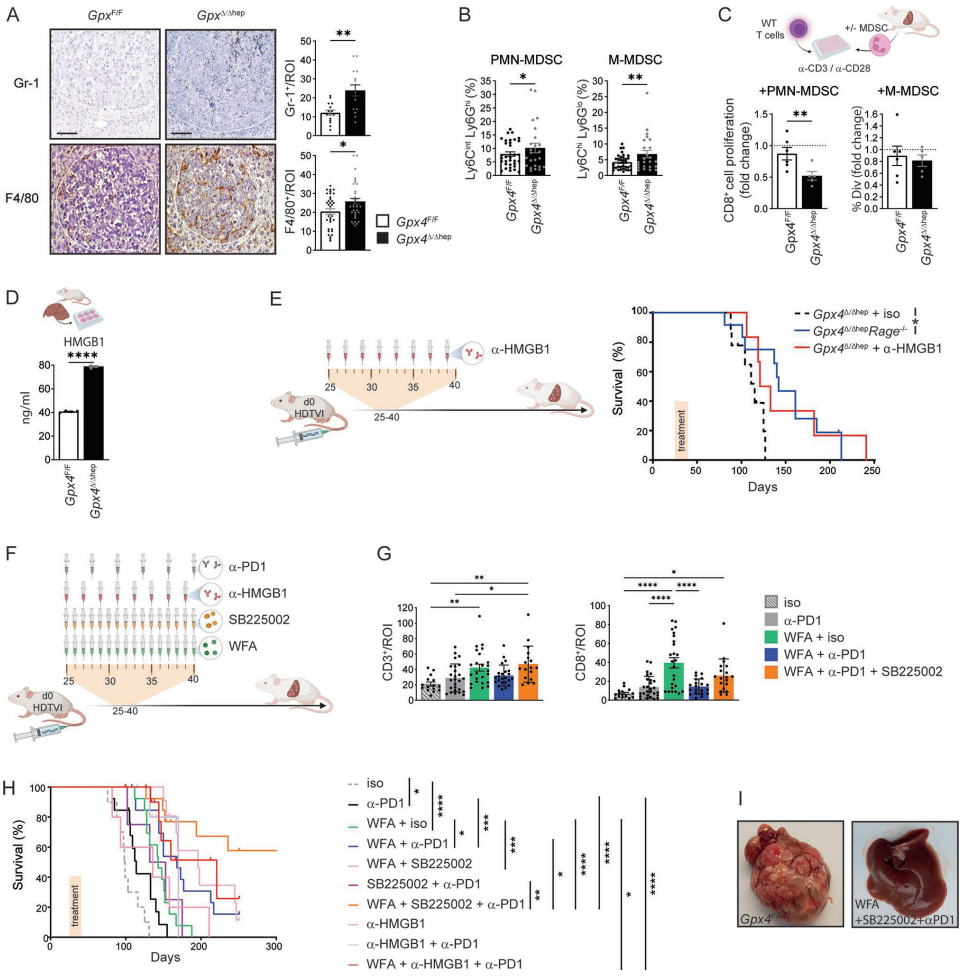

Figure 3 T cell activation and MDSC tumour infiltration induced by ferroptosis serve as targets for combinatory therapy for HCC. (A) Immunohistochemical analysis of Gr-1$^+$ (n=15) and F4/80$^+$ (n=35) cells in *Gpx4*$^{F/F}$ and *Gpx4*$^{\Delta/\Delta hep}$ HCC tumours. scale bars=100 µm. (B) Flow cytometry quantification of the percentages of PMN-MDSC and M-MDSC within the CD45$^+$infiltrates of livers from *Gpx4*$^{F/F}$ and *Gpx4*$^{\Delta/\Delta hep}$ HCC tumour-bearing mice. (n≥22). (C) Immunosuppression of MDSC isolated from livers of *Gpx4*$^{F/F}$ and *Gpx4*$^{\Delta/\Delta hep}$ tumour bearing mice on CD8$^+$ T cell proliferation. Fold change of the percentages of divided CD8$^+$ T cells with MDSC to CD8$^+$ T cells without MDSC (n≥5). (D) HMGB1 release by primary hepatocytes from *Gpx4*$^{F/F}$ and *Gpx4*$^{\Delta/\Delta hep}$ mice ex vivo for 4 hours (n=2). (E) Survival of *Gpx4*$^{\Delta/\Delta hep}$ mice treated with isotype Rat IgG2a,κ (as in 2J, n=9) or α-HMGB1 (n=6) and untreated *Gpx4*$^{\Delta/\Delta hep}$*/Rage*$^{-/-}$ (n=12) mice after HTVI. (F) Treatment scheme with i.p. injections of 250 µg of α-PD-1 or isotype (Rat IgG2a,κ), 50 µg of α-HMGB1, 2.5 mg/kg of WFA or 1 mg/kg of SB225002. (G) Immunohistochemical analysis of CD3$^+$ or CD8$^+$ T cell infiltration in HCC tumours of *Gpx4*$^{F/F}$ and *Gpx4*$^{\Delta/\Delta hep}$ mice>100 days after HTVI (n≥15). (H) Survival of WT mice after HTVI receiving Isotype (Rat IgG2a,κ) (n=10), α-PD-1 (n=13) (as in figure 2), WFA+isotype (Rat IgG2a,κ) (n=13), WFA + α-PD-1(n=14), WFA+SB225002 (n=12), SB225002 + α-PD-1 (n=13), WFA+SB225002 + α-PD-1 (n=14), α-HMGB1 (n=5), α-HMGB1 + α-PD1 (n=6) or WFA + α-HMGB1 + α-PD1 (n=12) treatments. (I) Pictures of livers of untreated *Gpx4*$^{F/F}$ mice at end point and WT mice treated with WFA+SB225002+α-PD-1 >300 days after HTVI. (A–H) Data are mean±SEM, *p≤0.05, **p≤0.01, ***p≤0.001, ****p≤0.0001 by t-test (A–D) one-way ANOVA with Šídák's's multiple comparisons of all groups (G) or by log-rank (Mantel-Cox) test (E, H). ANOVA, analysis of variance; HCC, hepatocellular carcinoma; HTVI, hydrodynamic tail vein injection; MDSC, myeloid derived suppressor cell; WFA, withaferin A.

113 to 127 days (p=0,0816), *Rage* deletion prolonged overall survival of *Gpx4*$^{\Delta/\Delta hep}$ mice significantly (figure 3E), yet in both cases some mice survived more than 200 days highlighting the tumour promoting role of MDSC on ferroptosis induction and supporting the notion that ferroptosis-associated HMGB1 release mediated infiltration of immunosuppressive PMN-MDSCs and M-MDSC counteracted a cytotoxic T cell response.

Considering that both blocking PD-1 or MDSC recruitment prolonged survival of *Gpx4*$^{\Delta/\Delta hep}$ mice with HCC, we wanted to examine whether pharmacological ferroptosis induction while targeting both immunosuppressive pathways, MDSCs and PD-1, could represent a therapeutic option for HCC treatment. To this end we generated liver tumours in WT mice and treated with WFA, a natural anticancer agent shown to induce ferroptosis by lipid peroxidation in vivo.[11] Additionally, mice were treated either with α−PD-1, the α−HMGB1 neutralising antibody or alternatively the CXCR2 inhibitor SB225002, a potent blocker of myeloid cell recruitment.[29] Tumour-bearing mice were treated for only 2 weeks starting on day 25 of the model (figure 3F). Analysis of CD3$^+$ and CD8$^+$ T cell infiltration in hepatic tumours after more than 100 days demonstrated that WFA treatment resulted in a long-lasting T cell infiltration, while blocking PD-1 alone or in combination with other compounds did not enhance T cell infiltration further (figure 3G) underlining the important contribution of ferroptosis for intratumoural T cell infiltration. While single administration of α-PD-1 improved survival by only 14.5 days, WFA monotreatment prolonged median survival by 44.5 days, yet the combination of these two was even more

effective (figure 3H) further supporting the notion that ferroptosis sensitises for checkpoint inhibition. However, when HMGB1 was blocked additionally, 50% of mice survived more than 200 days (online supplemental figure 3D). Treatment with α-HMGB1 significantly improved survival only when combined with WFA and α-PD-1 compared with WFA or α-PD-1 monotherapies (online supplemental figure 3D). However, employing SB225002 to block MDSC infiltration instead of α-HMGB1 along with both WFA and αPD-1 led to better survival rates. Indeed, the triple combination of WFA, α-PD-1 and SB225002 led to survival of 60% of mice for more than 300 days at which time livers were completely tumour free (figure 3H,I). Thus, although given only over a period of 2 weeks, the treatments provided a long-lasting effect in this highly aggressive model. Collectively, these data emphasise the need of targeting MDSCs to achieve the full potential of ferroptosis induction and PD-1 blockade.

Ferroptosis-associated cytotoxic T cell response provides tumour suppression only in liver

To examine whether tumour cell ferroptosis would trigger a comparable anti-tumour immune response also in other tumour entities, we took advantage of recently developed colorectal tumour organoids mutant for *Apc*, *Trp53*, *Tgfbr2*, *K-ras*^{G12D} (APTK) or additionally expressing a myristoylated AKT (APTKA) that can be transplanted into immunocompetent mice.[30 31] Doxycycline inducible shRNAs targeting *Gpx4* or control shRNA were introduced in both APTK and APTKA organoids and subcutaneous (s.c.) tumours were generated. Loss of Gpx4 protein expression and CD71 upregulation as a marker for ferroptosis induction in APTKA and APTK s.c. tumours expressing sh*Gpx4* were confirmed by immunohistochemistry (figure 4A,B and data not shown). Like in the HCC model loss of *Gpx4* alone did not affect tumour growth of s.c. colorectal tumours (figure 4C), yet flow cytometric analysis confirmed enhanced CD4$^+$ and CD8$^+$ T cell infiltration (online supplemental figure 4A) accompanied by increased IFNγ secretion by CD8$^+$ T cells (figure 4D) in *Gpx4*-deficient tumours that were further characterised by a T cell-dependent PD-L1 upregulation (figure 4E). CD8$^+$ T cells did not reveal any significant changes in the expression of CD69, PD-1, TIM3, CTLA-4 or Lag3 (online supplemental figure 4B). Similar to HCC, TAMs were not increased in Gpx4-deficient colorectal tumours, while DC and M-MDSC infiltration was enhanced (figure 4F). However, in contrast to the HCC model, PMN-MDSC infiltration was markedly reduced in the s.c. colorectal organoid-induced tumours (figure 4F). To evaluate whether the triple combination of pharmacological ferroptosis induction, MDSC suppression and checkpoint blockade could be successfully transferred to colorectal tumours, we treated APTKA or APTK tumours starting on day 7 for 2 weeks with WFA, SB225002 and α-PD-1. However, in contrast to HCC treatment the triple combination did not reduce primary colorectal tumour growth (figure 4G,H). To examine whether the lack of treatment response was due to the different tumour entity (colon vs HCC), the different underlying mutational spectrum or because tumours were treated outside the liver, we treated s.c. tumours derived from tumour cells that had been generated by HTVI of Nras^{G12V} and *myr*AKT in *p19*$^{-/-}$ mice.[32] However, the combined administration of WFA, α-PD-1 and SB225002 did not impair growth of these s.c. HCC established outside the liver (figure 4I,J) suggesting that sensitivity to triple therapy was defined by the tumour microenvironment rather than the tumour entity or the genetic profile. To confirm this, we refined a model of liver metastasis[33] and injected 50 000 APTK organoids into the spleen, which led to the development of liver metastases within 5 days at which point we initiated treatment (figure 4K). The individual administration of either SB225002, α-PD-1 or WFA alone did not affect the number of liver metastases (figure 4L). However, as expected, the combination of all three compounds significantly reduced the number of colorectal liver metastasis (figure 4L). Similarly, liver tumours induced by intrasplenic injection of 15 000 Nras^{G12V}/*myr*AKT/*p19*$^{-/-}$ HCC cells (figure 4M) responded well to the combination of SB225002, α−PD-1 and WFA (figure 4N). Collectively, these data highlight the niche specific immune response to ferroptosis and suggest that treatment of both primary liver tumours as well as liver metastases might benefit from a triple combination inducing ferroptosis and supporting cytotoxic T cell function.

DISCUSSION

Cytotoxic CD8$^+$ T cells have the capacity to trigger tumour cell ferroptosis,[16] however, here we place ferroptosis upstream of immune cell activation and demonstrate that hepatocyte ferroptosis due to genetic *Gpx4* ablation causes a complex immune response including enhanced CD8$^+$ T cell recruitment as well as an immunosuppressive response that counteracts T cell activation. Induction of an adaptive T cell response in the context of cell death has led to the concept of immunogenic cell death.[34] However, generalisation of such concept has been questioned and several studies have shown that the inflammatory response to cell death does not necessarily lead to a strong adaptive immune response.[35 36] Our data challenge such generalisation further and highlight the complex balance between T cell activation and suppression that is even context dependent. Ferroptosis in the liver induced an antitumour response while simultaneously triggering two immunosuppressive pathways counterbalancing cytotoxic T cells. Ferroptotic hepatocytes released CXCL10, which in turn stimulated CD8$^+$ T cell infiltration into the tumour. CXCL10 release was dependent on the activation of the cGAS/STING pathway most likely due to 8-OHdG accumulation in *Gpx4*$^{Δ/Δhep}$ ferroptotic tumours as previously described for pancreatic cancer.[18] Ferroptosis did not only trigger CD8$^+$ T cell infiltration, but also induced IFNγ secretion by CD8$^+$ T cells, which caused enhanced PD-L1 expression on tumour cells. Moreover, by releasing HMGB1, ferroptosis induced MDSC infiltration in combination with PD-L1 upregulation shielded tumour cells from the ferroptosis-induced CD8 dependent antitumour activity. While histological analysis of livers suggested an increase of F4/80$^+$ TAMs, we could not validate this by flow cytometry. Therefore, the ferroptosis' effect on myeloid immunosuppressive cells seemed to be limited to MDSC whose immunosuppressive activity[37] was confirmed in an ex vivo T cell proliferation assay. Intriguingly, we could not find any significance difference in activation and exhaustion surface marker expression levels on CD8$^+$ T cells from Gpx4-deficient ferroptotic tumours or control tumours. It is surprising that T cells submitted to such a high immunosuppressive environment, with PD-L1 upregulation and MDSC activity, did not succumb to exhaustion, but on the contrary are more prone to secrete IFNγ. Further analysis will be required to understand CD8$^+$ T cell resistance to exhaustion in the context of ferroptosis.

This dichotomy and orchestrated response of inhibitory and activation signals has been extensively studied and well described for acute viral infection and T cell activation, where T cell activation is commonly associated with upregulation of inhibitory pathways to tune down T cell activation in the contraction phase

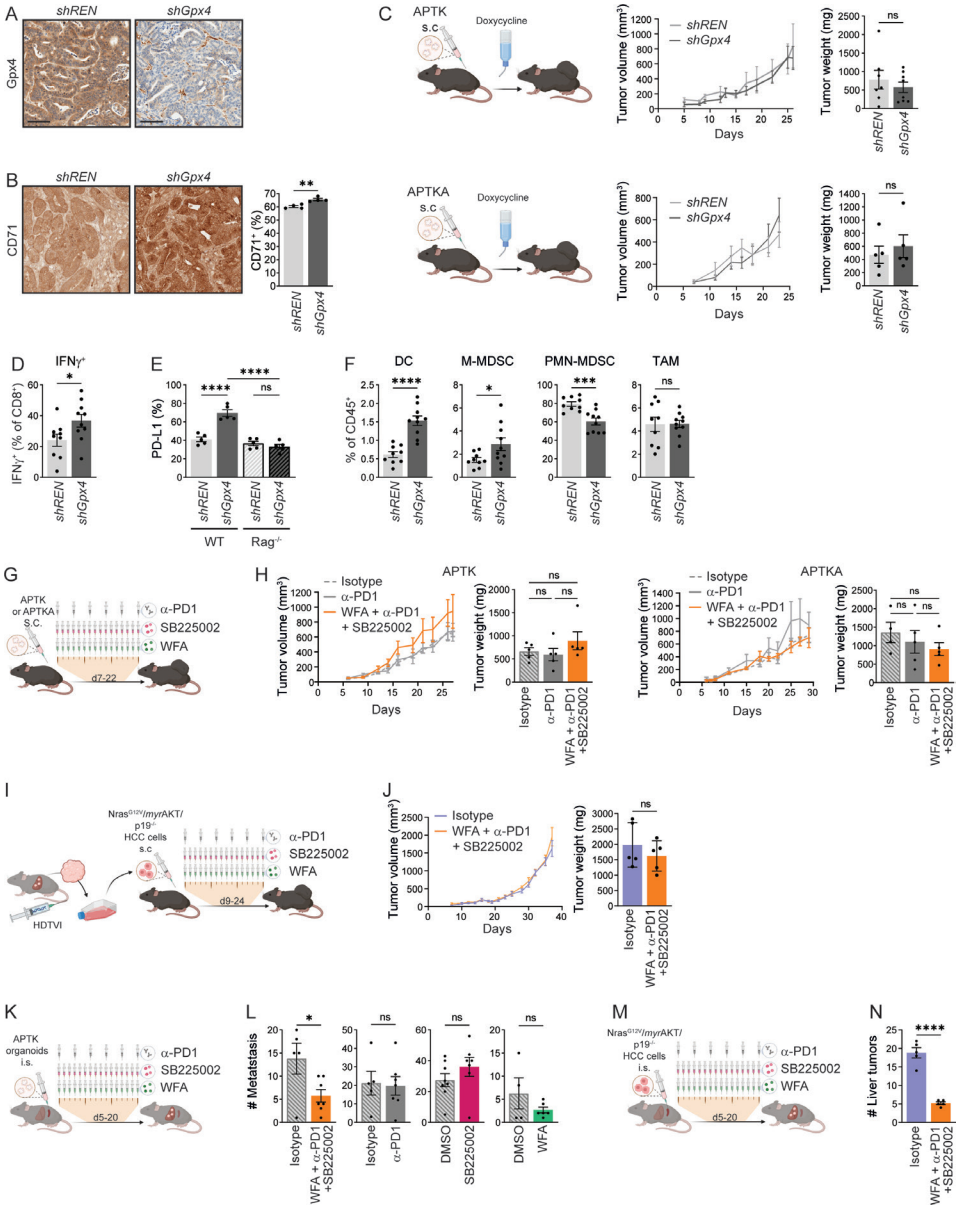

Figure 4 Ferroptosis effect on colorectal cancer. (A) Representative immunohistochemical Gpx4 staining of *shREN* or *shGPX4* APTKA s.c tumours. (B) Immunohistochemical quantification of $CD71^+$ cells in *shREN* and *shGpx4* APTKA s.c. tumours (n=4). (C) Tumour volumes and weights at end point of *shREN* and *shGpx4* APTK and ATPKA subcutaneous tumours (n≥5). (D) Flow cytometry analysis of IFNγ expression in $CD8^+$ T cells from *shREN* and *shGpx4* s.c. APTKA tumours, after ex vivo PMA/Ionomycin stimulation (n≥9). (E) Immunofluorescence quantification of PD-L1 expression in s.c *shREN* and *shGpx4* APTKA tumours from WT or $Rag^{-/-}$ mice (n=5). (F) Percentages of DC, M-MDSC, PMN-MDSC in immune infiltrates of *shREN* and *shGpx4* s.c. APTKA tumours analysed by flow cytometry (n≥9). (G) Treatment scheme after s.c. transplantation of APTK or APTKA organoids. (H) Tumour volumes and end point weights of s.c APTK and APTKA treated with the indicated compounds (n≥5). (I) Scheme for the isolation of $Nras^{G12V}$/*myr*AKT/$p19^{-/-}$ HCC cells followed by subcutaneous transplantation and treatments. (J) Tumour volumes and weights at end-point of subcutaneously transplanted $Nras^{G12V}$/*myr*AKT/$p19^{-/-}$ HCC cells with the indicated treatment. (K) Treatment scheme after intrasplenic (i.s.) injection of APTK organoids. (L) Numbers of liver metastasis after intrasplenic injection of APTK organoids and treatment as indicated (n≥4). (M) Treatment scheme after intrasplenic (i.s.) injection of $Nras^{G12V}$/*myr*AKT/$p19^{-/-}$ HCC cells. (N) Number of liver tumours after intrasplenic transplantation of $Nras^{G12V}$/*myr*AKT/$p19^{-/-}$ HCC cells and the indicated treatment (n≥5). (G, I, K, M) Scheme for i.p. injections, each represented by a syringe, with 250 µg of α-PD-1 or isotype (Rat IgG2a,κ), 2.5 mg/kg of Withaferin A (WFA) or 1 mg/kg of SB225002. (B–M) Data are mean±SEM, n.s not significant, *p≤0.05, ***p≤0.001, ****p≤0.0001 by t-test (B–F, J, L, N) one-way ANOVA with Šídák's multiple comparisons test (H) of the indicated pairs. ANOVA, analysis of variance; DC, dendritic cell; HCC, hepatocellular carcinoma; MDSC, myeloid derived suppressor cell; PMA, phorbol myristate acetate; s.c., subcutaneous.

and safeguard against 'self'-directed T cell activity. Therefore, in the context of immune-based cancer treatments a comprehensive analysis of the immune response needs to be implemented in order to identify potent anticancer agents whose antitumourigenic function would be masked by immunosuppressive activity that could be overcome by the right combinatorial treatment. We identified ferroptosis as such an example, where T cell activation is accompanied by PD-L1 and MDSC driven immunosuppression.

Importantly, T cell recruitment and consequent PD-L1 upregulation were observed in both models of primary HCC and colorectal cancer (CRC). However, while PD-1 blockade in HCC conferred a survival benefit, this was not the case in s.c. colorectal tumours. Also, the triple combination of WFA, SB225002 and α-PD-1 was only successful when liver tumours or metastases were treated, primary CRC did not respond to this approach. This suggests that the ferroptosis-induced immune response is not a general one but rather depends on the respective local microenvironment. Interestingly, in s.c. CRC we could not observe the pronounced PMN-MDSC accumulation we noticed in liver. Yet, this alone would not explain the unresponsiveness to checkpoint blockade of primary CRC tumours indicating that additional cellular mechanisms control immune response. Cancer-associated fibroblasts (CAFs) that are characterised by a high degree of heterogeneity may play an important role in this context as we have recently shown their potential to dictate the response to radiotherapy.[31] An important open question is the degree of interdependency between cancer cells, through their mutations, (neo)antigens, surface protein expression and secretome and the tumour environment. Our data demonstrate that the combination of inducing ferroptosis along with PD-1 and MDSC blockade does not rely on the presence of a particular tumour cell specific mutation and therefore such combination therapy could potentially be applied to any tumour type where the therapy's efficacy would be determined by the tumour microenvironment response to ferroptosis. Moreover, the individual components of a combination therapy could be adapted to the tumour environment with the ferroptosis inducing agent and α-PD-1 therapy as a basis. For management of liver cancers and CRC liver metastases, we illustrate that adding MDSC blockade is sufficient to establish a proper tumour suppression. For a direct clinical translation of our findings one should consider the caveat that we did not assess responsiveness of human HCC (different types or stages). Nevertheless, our data strongly suggest that the sensitivity of the primary tumour to this approach is irrelevant for the response of liver metastases of the same genetic background suggesting that such combinatorial treatment may be effective to treat liver metastases emerging from any cancer type.

Collectively, our data illustrate the complex interplay of tumour cell ferroptosis and adaptive immunity that provide the rationale for an innovative combinatorial treatment of primary liver tumours and metastases.

Author affiliations
[1]Institute for Tumor Biology and Experimental Therapy, Georg-Speyer-Haus, Frankfurt/Main, Germany
[2]Frankfurt Cancer Institute, Goethe University Frankfurt, Frankfurt/Main, Germany
[3]Department of Medicine I, Gastroenterology, Hepatology and Endocrinology, Goethe University Frankfurt, Frankfurt/Main, Germany
[4]University Medical Center Göttingen (UMG), Institute of Human Genetics, NGS-Integrative Genomics Core Unit (NIG), Göttingen, Germany
[5]Institute of Pathology, UniversitätsKlinikum Heidelberg, Heidelberg, Germany
[6]Center for Biomedical Science, The Feinstein Institute for Medical Research, Manhasset, New York, USA
[7]German Cancer Consortium (DKTK) and German Cancer Research Center (DKFZ), Heidelberg, Germany

Twitter Dominic Denk @DomDenkMD

Acknowledgements We thank Eva Rudolf, Preeti Gupta and Christin Danneil for expert technical assistance as well as the staff at the Animal Facility and the Histology and Flow Cytometry Core Facilities at the Georg-Speyer-Haus. We are grateful to Marcus Conrad for providing floxed Gpx4 mice as well as Daniel Dauch for providing murine liver tumour cell lines and thank Thomas Pleli for help with primary hepatocyte cultures. We thank the Else-Kröner-Fresenius-Stiftung (EKFS) for supporting his work.Graphical experimental schemes were created with BioRender.com.

Contributors CC, FF, DD, AN, KK, TWB, EE, YD and KM performed in vivo experiments and collected tissues samples. CC, FF, DD, KK, MP and TWB performed ex vivo experiments including the primary hepatocytes isolation and flow cytometry analysis. FF, CC, AN, FC and ÖC performed and analysed the IHC and IF staining. FF and ÖC performed qPCR experiments and analysis. GS performed RNAseq experiments. K-HP, SZ and TL provided support and expertise in the field of HCC. TL provided pathological assessment of liver histology. HY generated and provided the α-HMGB1 antibody for in vivo treatment. FRG conceptualised and supervised the study. CC, FF and FRG wrote the manuscript. FRG acts as guarantor.

Funding FF was supported by the 'Patenschaftsmodell' of the Goethe University Frankfurt and the Else-Kröner-Forschungskolleg. Work in the lab of FRG is supported by institutional funds from the Georg-Speyer-Haus, by the LOEWE Center Frankfurt Cancer Institute (FCI) funded by the Hessen State Ministry for Higher Education, Research and the Arts [III L 5 - 519/03/03.001 - (0015)], Deutsche Forschungsgemeinschaft (FOR2438: Gr1916/11-1; SFB1292-Project ID: 318346496-TP16; SFB1479-Project ID: 441891347-P02; GRK2336) and the ERC (Advanced Grant PLASTICAN-101021078). The Institute for Tumor Biology and Experimental Therapy, Georg-Speyer-Haus, is funded jointly by the German Federal Ministry of Health and the Ministry of Higher Education, Research and the Arts of the State of Hessen (HMWK).

Competing interests None declared.

Patient and public involvement Patients and/or the public were not involved in the design, or conduct, or reporting, or dissemination plans of this research.

Patient consent for publication Not applicable.

Provenance and peer review Not commissioned; externally peer reviewed.

Data availability statement Data are available on reasonable request. All data relevant to the study are included in the article or uploaded as online supplemental information.

ORCID iDs
Fabian Finkelmeier http://orcid.org/0000-0001-8559-9910
Kai-Henrik Peiffer http://orcid.org/0000-0002-3757-4476
Thomas Longerich http://orcid.org/0000-0001-8888-1030
Florian R Greten http://orcid.org/0000-0002-3928-6080

REFERENCES

1 Dixon SJ, Lemberg KM, Lamprecht MR, *et al*. Ferroptosis: an iron-dependent form of nonapoptotic cell death. *Cell* 2012;149:1060–72.
2 Fellmann C, Hoffmann T, Sridhar V, *et al*. An optimized microRNA backbone for effective single-copy RNAi. *Cell Rep* 2013;5:1704–13.
3 Chen X, Kang R, Kroemer G, *et al*. Ferroptosis in infection, inflammation, and immunity. *J Exp Med* 2021;218:e20210518.
4 Ursini F, Maiorino M, Valente M, *et al*. Purification from pig liver of a protein which protects liposomes and biomembranes from peroxidative degradation and exhibits glutathione peroxidase activity on phosphatidylcholine hydroperoxides. *Biochim Biophys Acta* 1982;710:197–211.

5 Friedmann Angeli JP, Krysko DV, Conrad M. Ferroptosis at the crossroads of cancer-acquired drug resistance and immune evasion. *Nat Rev Cancer* 2019;19:405–14.
6 Jiang L, Kon N, Li T, *et al*. Ferroptosis as a p53-mediated activity during tumour suppression. *Nature* 2015;520:57–62.
7 Zhang Y, Shi J, Liu X, *et al*. Bap1 links metabolic regulation of ferroptosis to tumour suppression. *Nat Cell Biol* 2018;20:1181–92.
8 Li J, Cao F, Yin H-L, *et al*. Ferroptosis: past, present and future. *Cell Death Dis* 2020;11:88.
9 Louandre C, Marcq I, Bouhlal H, *et al*. The retinoblastoma (Rb) protein regulates ferroptosis induced by sorafenib in human hepatocellular carcinoma cells. *Cancer Lett* 2015;356:971–7.
10 Ye Z, Liu W, Zhuo Q, *et al*. Ferroptosis: final destination for cancer? *Cell Prolif* 2020;53:e12761.
11 Hassannia B, Wiernicki B, Ingold I, *et al*. Nano-targeted induction of dual ferroptotic mechanisms eradicates high-risk neuroblastoma. *J Clin Invest* 2018;128:3341–55.
12 Mao L, Zhao T, Song Y, *et al*. The emerging role of ferroptosis in non-cancer liver diseases: hype or increasing hope? *Cell Death Dis* 2020;11:518.
13 Louandre C, Ezzoukhry Z, Godin C, *et al*. Iron-Dependent cell death of hepatocellular carcinoma cells exposed to sorafenib. *Int J Cancer* 2013;133:1732–42.
14 Jia M, Zhang H, Qin Q, *et al*. Ferroptosis as a new therapeutic opportunity for nonviral liver disease. *Eur J Pharmacol* 2021;908:174319.
15 Chen X, Kang R, Kroemer G, *et al*. Targeting ferroptosis in pancreatic cancer: a double-edged sword. *Trends Cancer* 2021;7:891–901.
16 Wang W, Green M, Choi JE, *et al*. $CD8^+$ T cells regulate tumour ferroptosis during cancer immunotherapy. *Nature* 2019;569:270–4.
17 Liao P, Wang W, Wang W, *et al*. $CD8^+$ T cells and fatty acids orchestrate tumor ferroptosis and immunity via ACSL4. *Cancer Cell* 2022;40:365–78.
18 Dai E, Han L, Liu J, *et al*. Ferroptotic damage promotes pancreatic tumorigenesis through a TMEM173/STING-dependent DNA sensor pathway. *Nat Commun* 2020;11:6339.
19 Dai E, Han L, Liu J, *et al*. Autophagy-Dependent ferroptosis drives tumor-associated macrophage polarization via release and uptake of oncogenic KRAS protein. *Autophagy* 2020;16:2069–83.
20 Efimova I, Catanzaro E, Van der Meeren L, *et al*. Vaccination with early ferroptotic cancer cells induces efficient antitumor immunity. *J Immunother Cancer* 2020;8:e001369.
21 Carlson CM, Frandsen JL, Kirchhof N, *et al*. Somatic integration of an oncogene-harboring sleeping Beauty transposon models liver tumor development in the mouse. *Proc Natl Acad Sci U S A* 2005;102:17059–64.
22 Canli Özge, Alankuş YB, Grootjans S, *et al*. Glutathione peroxidase 4 prevents necroptosis in mouse erythroid precursors. *Blood* 2016;127:139–48.
23 Carlson BA, Tobe R, Yefremova E, *et al*. Glutathione peroxidase 4 and vitamin E cooperatively prevent hepatocellular degeneration. *Redox Biol* 2016;9:22–31.
24 Feng H, Schorpp K, Jin J, *et al*. Transferrin receptor is a specific ferroptosis marker. *Cell Rep* 2020;30:3411–23.
25 Greten FR, Grivennikov SI. Inflammation and cancer: triggers, mechanisms, and consequences. *Immunity* 2019;51:27–41.
26 Rudalska R, Dauch D, Longerich T, *et al*. In vivo RNAi screening identifies a mechanism of sorafenib resistance in liver cancer. *Nat Med* 2014;20:1138–46.
27 Mowat C, Mosley SR, Namdar A, *et al*. Anti-Tumor immunity in mismatch repair-deficient colorectal cancers requires type I IFN-driven CCL5 and CXCL10. *J Exp Med* 2021;218:e20210108.
28 Li J, Sun J, Rong R, *et al*. Hmgb1 promotes myeloid-derived suppressor cells and renal cell carcinoma immune escape. *Oncotarget* 2017;8:63290–8.
29 Highfill SL, Cui Y, Giles AJ, *et al*. Disruption of CXCR2-mediated MDSC tumor trafficking enhances anti-PD1 efficacy. *Sci Transl Med* 2014;6:237ra67.
30 Varga J, Nicolas A, Petrocelli V, *et al*. Akt-Dependent Notch3 activation drives tumor progression in a model of mesenchymal colorectal cancer. *J Exp Med* 2020;217:e20191515.
31 Nicolas AM, Pesic M, Engel E, *et al*. Inflammatory fibroblasts mediate resistance to neoadjuvant therapy in rectal cancer. *Cancer Cell* 2022;40:168–84.
32 Seehawer M, Heinzmann F, D'Artista L, *et al*. Author correction: necroptosis microenvironment directs lineage commitment in liver cancer. *Nature* 2018;564:E9.
33 Soares KC, Foley K, Olino K, *et al*. A preclinical murine model of hepatic metastases. *J Vis Exp* 2014;51677:51677.
34 Galluzzi L, Buqué A, Kepp O, *et al*. Immunogenic cell death in cancer and infectious disease. *Nat Rev Immunol* 2017;17:97–111.
35 Ciampricotti M, Hau C-S, Doornebal CW, *et al*. Chemotherapy response of spontaneous mammary tumors is independent of the adaptive immune system. *Nat Med* 2012;18:344–6. author reply 6.
36 Hou J, Greten TF, Xia Q. Immunosuppressive cell death in cancer. *Nat Rev Immunol* 2017;17:401.
37 Bronte V, Brandau S, Chen S-H, *et al*. Recommendations for myeloid-derived suppressor cell Nomenclature and characterization standards. *Nat Commun* 2016;7:12150.

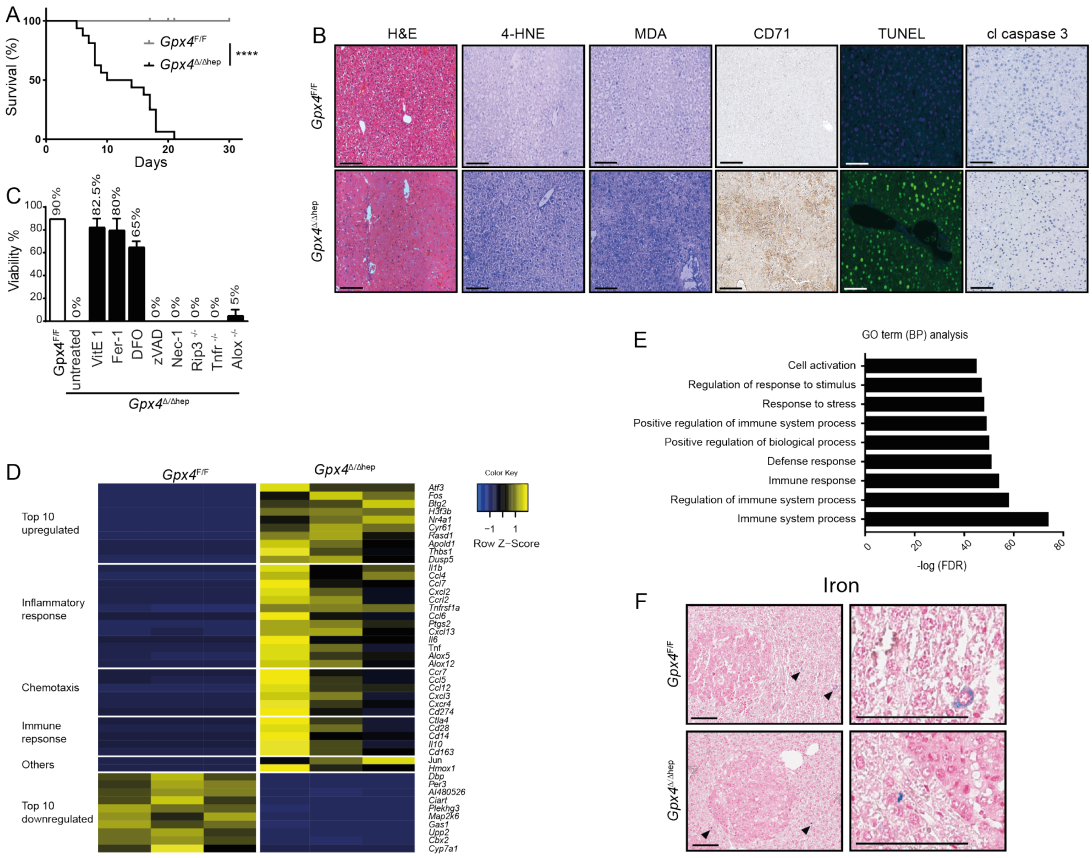

Supplemental figure 1: *Gpx4* deletion in hepatocytes causes ferroptosis and inflammation.

A, Survival of *Gpx4*$^{F/F}$ and *Gpx4*$^{\Delta/\Delta hep}$ mice placed on a vitamin E-depleted diet (n=9) ****p≤0,0001 by log-rank (Mantel-Cox) test.

B, Representative H&E, 4-HNE, MDA, TUNEL and cleaved caspase 3 staining of livers from *Gpx4*$^{F/F}$ and *Gpx4*$^{\Delta/\Delta hep}$ mice fed with vitamin E-depleted diet.

C, Viability of primary hepatocytes from *Gpx4*$^{F/F}$, *Gpx4*$^{\Delta/\Delta hep}$, *Gpx4*$^{\Delta/\Delta hep}$/*Rip3*$^{-/-}$, *Gpx4*$^{\Delta/\Delta hep}$/*Tnfr1*$^{-/-}$ and *Gpx4*$^{\Delta/\Delta hep}$/*Alox*$^{-/-}$ mice cultured for 24 hours *ex vivo* left either untreated or in the presence of vitamin E (VitE), ferrostatin-1 (Fer-1), deferoxamine (DFO), zVAD or necrostatin-1 (Nec-1), Data are ± SD (n=2).

D, Heatmap of the most differentially expressed genes in livers from *Gpx4*$^{F/F}$ and *Gpx4*$^{\Delta/\Delta hep}$ mice fed with vitamin E-depleted diet (n=3).

E, GOterm biological process analysis of *Gpx4*$^{F/F}$ and *Gpx4*$^{\Delta/\Delta hep}$ mice fed with vitamin E-depleted diet (n=3).

F, Representative images with zoomed in of iron staining of the liver of HCC bearing *Gpx4*$^{F/F}$ and *Gpx4*$^{\Delta/\Delta hep}$ mice 25 days after HTVI. Scale bars = 100µm.

Conche C, *et al. Gut* 2023;0:1–9. doi: 10.1136/gutjnl-2022-327909

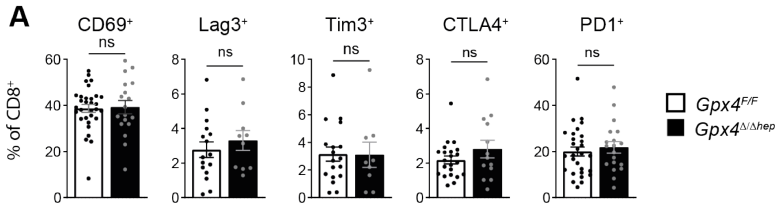

Supplemental figure 2

A, Flow cytometry analysis of the indicated surface markers on CD8 T cells from liver infiltrates of *Gpx4*$^{F/F}$ and *Gpx4*$^{\Delta/\Delta hep}$ of tumor bearing mice (n≥7). Data are mean ±SEM, n.s not significant by t test.

Conche C, *et al. Gut* 2023;0:1–9. doi: 10.1136/gutjnl-2022-327909

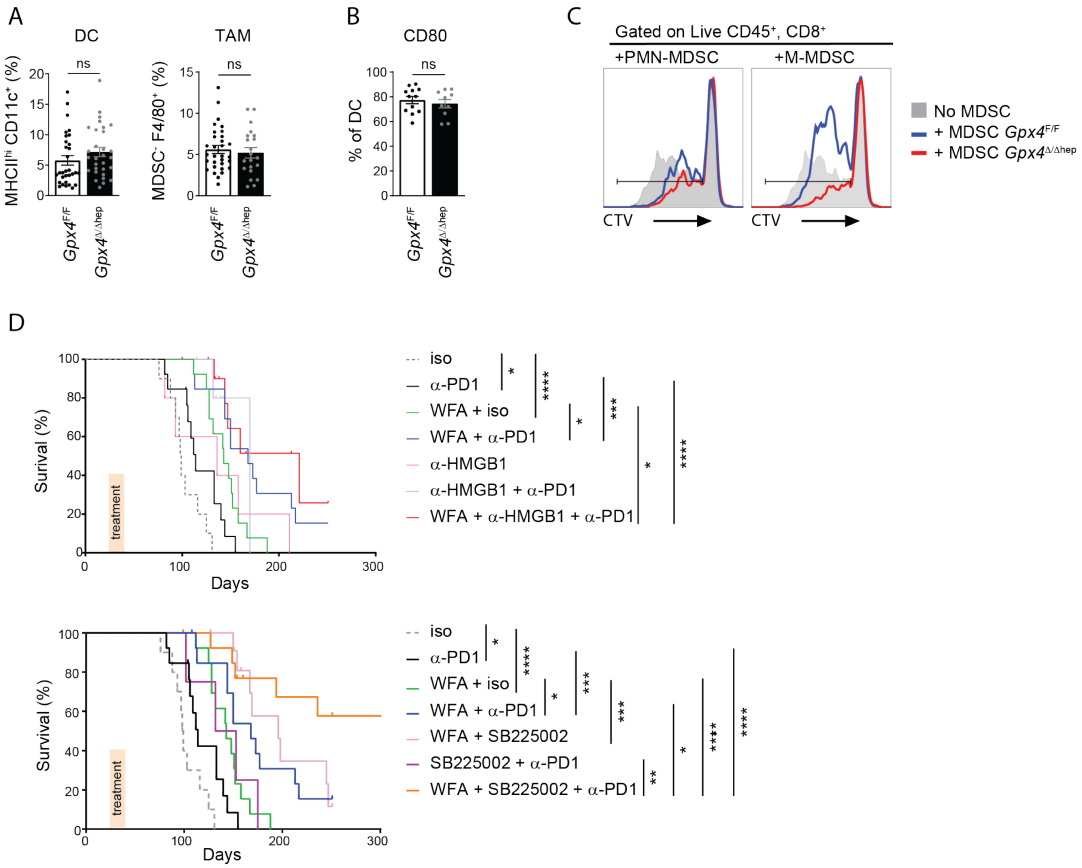

Supplemental figure 3

A, Quantification by flow cytometry analysis of DC and TAM liver infiltrates of *Gpx4*$^{F/F}$ and *Gpx4*$^{\Delta/\Delta hep}$ tumor bearing mice (n≥21). Data are mean ±SEM, n.s, not significant, **p≤0,01, by t test.

B, Quantification by flow cytometry analysis of activation marker CD80 expression on DC of *Gpx4*$^{F/F}$ and *Gpx4*$^{\Delta/\Delta hep}$ tumor bearing mice (n≥10).

C, Representative Celltrace violet dilution profile of WT CD8 T cell proliferation without MDSC (solid grey) or incubated with tumor infiltrating MDSC from *Gpx4*$^{F/F}$ (Blue) and *Gpx4*$^{\Delta/\Delta hep}$ (red) mice.

D, Survival curves presented in figure 3H and separated into two graphs depending on according to MDSC blockade: α-HMGB1 vs SB225002.

A-D, Data are mean ±SEM, n.s, not significant, *p≤0,5, **p≤0,01, ***p≤0,001 and ****p≤0,0001by t test (**A-B**) or by log-rank (Mantel-Cox) test (**D**).

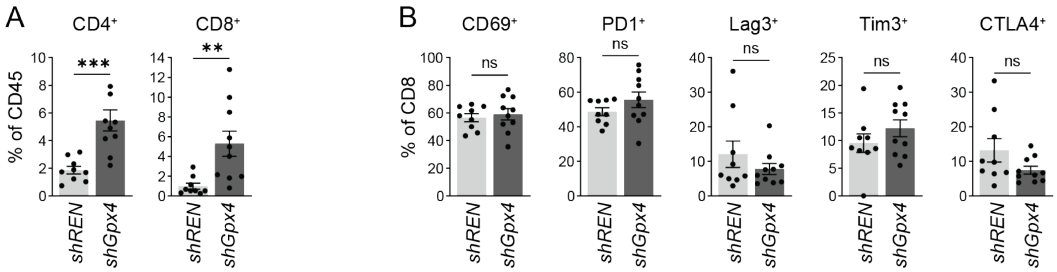

Supplemental figure 4

A, Quantification of the percentages of CD4 and CD8 T cells in immune infiltrates of *shREN* and *shGpx4* s.c. APTKA tumors analyzed by flow cytometry (n≥9).

B, Percentages of cells expressing the indicated surface markers on CD8 T cells in immune infiltrates of *shREN* and *shGpx4* s.c. APTKA tumors analyzed by flow cytometry (n≥9).

Methods

Mice

Gpx4$^{F/F}$ [1], *Tnfr1*$^{-/-}$(Jackson Laboratory, JAX:003242), *Rip3*$^{-/-}$[2], Alox12/15$^{-/-}$[3] and *Rage*$^{-/-}$ [4] mice were crossed to *Alb-Cre* mice (JAX:003574; Jackson Laboratory). FvB mice from Charles River and C57BL/6J mice Janvier were used. Mice were kept in a temperature-controlled room with 12 h light and 12 h dark diurnal cycle. They were housed in filter-topped cages and were standard laboratory chow and water ad libitum. All animal procedures were performed in accordance with institutional guidelines. All animal experiments were reviewed and approved by the Regierungspräsidium Darmstadt, Germany. No statistical method was used to predetermine sample size. Livers were photographed and sampled. Counting of tumors was done in a blinded fashion. Vitamin E–deficient diet was purchased from Ssniff (E15791-147).

Isolation of primary murine hepatocytes

Mice were anaesthetized with ketamine/rompune (100 mg/200 mg per kg body weight). Afterwards a cannula was inserted in the vena cava inferior for perfusion of the liver. The isolation procedure was adapted from [5]. Briefly, perfusion was performed with 37°C warm HBSS without Ca2+ and Mg2+ (supplemented with 15 mM HEPES, 2.5 mM EDTA, 1 g/l glucose, 100 U/ml penicillin and 100 µg/ml streptomycin, 1% non-essential amino acids) using a roller pump (10 ml/min) for 10 min. Thereafter, the liver was perfused with HBSS with Ca2+ and Mg2+ (supplemented with 15 mM HEPES, 5 mM CaCl2, 0.13 mg/ml collagenase IV (Sigma-Aldrich, C5138, Darmstadt, Germany), 100 U/ml penicillin, and 100 µg/ml streptomycin for additional 10 min. The liver was carefully removed from the abdominal cavity, placed in a Petri dish on ice in Williams E medium (supplemented with

10% FCS, 100 U/ml penicillin, and 100 µg/ml streptomycin) and opened with forceps. Liver cells were resuspended and put over a 100 µm cell strainer. Cells were washed and seeded in Williams Medium E (supplemented with 10% FCS, 2 mM L-Alanyl-L-Glutamin (Biochrom), 100 U/ml penicillin, and 100 µg/ml streptomycin) on collagen coated plates (Roche collagen rat tail).

For HMGB1 and CXL10 release, hepatocyte supernatants were collected after 4h.

For inhibitor treatment in Figure S1A adherent hepatocytes were washed after 4 h with PBS and fresh Williams Medium E (supplemented with 10% FCS, 2 mM L-Alanyl-L-Glutamin (Biochrom), 100 U/ml penicillin, and 100 µg/ml streptomycin). Vitamin E (T3251; Sigma), Necrostatin-1 (480065; Calbiochem), Ferrostatin-1(341494; Calbiochem), Deferroxamin (deferoxamine mesylate salt) (D9533; Sigma), Z-VAD (OMe)-FMK (Caspase Inhibitor-1) (627610; Calbiochem) were dissolved in DMSO, EtoH or PBS according to manufacturer suggestions and used in the described concentrations. Then inhibitors were dissolved in medium and changed after 4 hours and every 24 hours. For quantification of cell death, cells were trypsinized and stained with trypan blue followed by counting with a haemocytometer using standard protocol. Cells stained blue were considered as dead cells.

HCC cell lines.

HCC cell lines were generated as previously described [6]. Briefly, HTVI with $Nras^{G12V}$ and myristoylated-AKT (see Liver Tumor mouse model with Hydrodynamic tail vein injections) oncogenes in *p19*$^{-/-}$ mice given that *p19* deletion is required for HCC tumor cells to growth in vitro. Briefly, HCC nodules were digested and put in culture on agarose coated plates. Then cells were cultured in Advanced DMEM supplemented with 10% FCS, 100 U/ml penicillin, and 100 µg/ml streptomycin, 2mM Glutamax.

Organoid cell culture

APTK and APTKA organoids were established as previously described [7]. Organoids were expanded by manual disruption and seeded in Matrigel BME or Ultra-Matrix (Corning) with advanced DMEM/F12 supplemented with N2, B27, L-NAC and appropriate antibiotics. Gpx4 shRNA was cloned in RT3REN vector as described previously [8]. Rtta3-hygro retroviral vector was a kind gift from Lars Zender and RT3REN (Addgene plasmid # 111166) a kind gift from Johannes Zuber. TGCTGTTGACAGTGAGCGCAGGAATTATAATGCTTATCTATAGTGAAGCCACAGAT GTATAGATAAGCATTATAATTCCTATGCCTACTGCCTCGGA sequence was used for REN shRNA while TGCTGTTGACAGTGAGCGAAGGAAGTAATCAAGAAATCAATAGTGAAGCCACAGA TGTATTGATTTCTTGATTACTTCCTGTGCCTACTGCCTCGGA was used for shRNA targeting *Gpx4*. For transplantation organoids were mechanically disturbed and incubated for 5 to 10 min with accutase to generate single cell suspension.

Tumor mouse models

Liver Tumor mouse model with Hydrodynamic tail vein injections. For transposon-mediated intrahepatic gene transfer, mice received a 5:1 molar ratio of transposon- to transposase encoding vectors (30 μg total DNA). One transposon vector contains transposable elements encoding oncogenic $Nras^{G12V}$ and myristoylated-AKT with CAGGS promoter (Caggs), inverted repeats and direct repeats (IR/DR) and internal ribosome entry site (IRES) while the other vector encodes fror sleeping beauty (SB) transposase as depicted in (Figure 4A). DNA for hydrodynamic tail vein injection was prepared using Qiagen EndoFreeMaxi Kit

(Qiagen, Hilden, Germany) and dissolved in 0.9% NaCl solution to a final volume of 10% of animal's body weight. Animals (5-7 weeks old) were injected within 10 s with 25 μg transposon plasmids and 5 μg transposase. Transposon-based vector pCAGGs-IRES was used. For the survival study, human endpoint was reached when mice were lethargic or with reduced activity for 3 consecutive days without improvement. Some mice developed lesion on the ear, paws and mostly on the tails as described previously [9]. Following our animal experimentation protocol, mice with lesion at eminent risk of rupture or bleeding were euthanized. Any mouse that was sacrificed due to those lesions or for any health reason unrelated to liver tumor was censured at the time of sacrifice.

Subcutaneous tumor transplantation

Organoids or HCC cells were injected in 10-20% Matrigel into the right flank. Once all tumors reached a measurable size of 3-4mm, approximately 7 days after transplantation for organoids and 9 days for HCC cells treatment of the mice was initiated. For organoids encoding for shRNA, first shRNA expression was induced in vitro for several passages by adding 0,5μg/ml of doxycycline to the medium. Then, one day after s.c. transplantation, the drinking water was supplemented with 0,5μg/ml doxycycline and 3% sucrose. Tumor volumes were calculated with ½(width^2 x length).

For Liver metastasis model with intrasplenic injection [10], 50 000 single cell organoids or 15.000 HCC cells were injected into the spleen and treatment was initiated 5 days after transplantation. Due to the time required for the surgery, a limited number of mice could be injected. Therefore, only 2 treatment groups could be assessed by cohort. Mice that haven't developed any liver metastasis were considered as miss-injected and therefore excluded from analysis.

In vivo treatments

For treatment therapies, treatments were given for 16 days and initiated at different time point according to the tumor models. 250μg of α-PD-1 (CD279) monoclonal antibody (clone RMP1-14, BioXCell) or IgG2a isotype control was administered i.p. every 3 days for six injections. 50μg of α-HMBG1, obtained from Dr. Huan Yang, was injected i.p every other day for the tumor model and daily for the vitamin E depleted diet. Withaferin A (Sigma-Aldrich) and SB225002 (SelleckChem) were injected i.p. daily at 2,5mg/kg and 1mg/kg respectively. WFA, SB225002, αPD1 and αHMGB1 treatments were administrated at days 25 after HTVI, day 5 after intra-splenic injections, when s.c tumors were palpable, e.g. 7 days and when the orthotopic tumors reach ~2/3 of the colon lumen. For depletion of CD8 cells, mice were treated after HTVI weekly with 150μg of depleting α-CD8 or Rat IgG2b, κ antibodies for 3 consecutive days.

Histology and immunochemistry

For histological analysis tissue was fixed in 4% PFA or Formaline and paraffin embedded. After deparaffinization and rehydration of the tissue haematoxylin and eosin (H&E) staining was done according to standard protocols. Tumor number, size and tumor-to-liver ratio quantification was performed manually on H&E stained liver sections scanned on a Aperio CS2 (Leica). To determine cell proliferation, mice were injected i.p. with 75 mg/kg BrdU (Sigma-Aldrich) 90 min before sacrifice. For MDA (ab6463; Abcam), 8-OHdG (ab10802; Abcam) and 4-HNE (ab46545; Abcam) staining, paraffin sections were incubated in proteinase K for up to 40 minutes at 37C° for antigen retrieval. Alkaline phosphatase reaction was used as a color reaction with nuclear fast red (Sigma) as a nuclear counter stain. For Nras staining (sc-31; Santa Cruz) paraffin sections were incubated in proteinase K for up to 40

minutes at 37C° for antigen retrival and vector mouse on mouse Kit tumor (MOM PK-2200; Vector) used for staining. For CD71 (H68.4; Invitrogen) immunohistochemistry, slides were subjected to heat-induced antigen retrieval in Tris-EDTA (pH:9.0) solution for 15 min. Slides were blocked and treated with Transferrin Receptor primary antibody (H68.4; Invitrogen) using MOM kit according to the manufacturer`s instructions. Detection was performed with the DAB substrate kit (SK-4100; Vector). For α-F4/80 (ab6640; Abcam), α-GPx4 (ab125066; Abcam), α-BrdU (MCA2060; AbD Serotec), α-cleaved caspase 3 (9661S; Cell Signaling Technology), α-CD3 (IS503: DAKO), α-CD8 (98941; cell signaling), α-GR-1 (Ly6G) (11-5931-82; eBioscience), α-p-H2AX (9718; Cell Signaling Technologies) and Prussian Blue iron stain (Merck; 10498401000, paraffin sections were stained using a Leica Bond Max following standards immunochemistry staining protocols. 4-HNE, MDA, p-H2AXa, CD71 and 8-OHdG stained sections were scanned using Aperio CS2 (Leica). Quantification of 4-HNE, MDA, and CD71 was done using a membrane algorithm whereas quantification of 8-OHdG and p-H2AX was done using a nuclear staining algorithm (Aperio eSlide manager software) on manually marked tumors. For CD3, Gr-1, F4-80 and cleaved caspase 3, non-overlapping images within the tumor area were acquired with 20x objective and positive cells were counted manually. Histology allowed for the individual analysis of the multiple tumors generated by HTVI (see Figure 1 C) therefore n represented the number of tumors analyzed from at least 3 mice per group (Figure 1D, 2B, 3A, 3G)

Immunofluorescence

Terminal deoxynucleotidyl transferase deoxyuridine triphosphate nick-end labeling (TUNEL) assay was performed with the ApoAlert DNA Fragmentation Assay Kit (Clontech, 630107). Briefly, tissues were treated with 0,9% NaCl for 5 min, then with with 4% PFA for 5min

followed by an incubation for 30min with proteinase K for 5min. After being blocked for 10-15 min, sections were incubated with terminal deoxynucleotidyl transferase enzyme mix for 1h and then mounted in medium containing 4,6 diamidino-2-phenylindole. For CD8 and PD-L1 staining, Section were stained overnight with αPD-L1 (13684; Cell Signaling Technologies) or α-CD8 (361003; Synaptic Systems) after antigen retrieval with EDTA or Citrate Buffer respectively for 10min and followed by a AF594-coupled secondary antibody. Image acquisition was performed using a Zeiss Axio Imager M2 with a 20×/0.5 EC Plan Neofluar or a 40×/0.95 korr Apochromat objective. The images were captured on a Zeiss microscope and positive cells were quantified manually. Immunofluorescence allowed for the individual analysis of the multiple tumors generated by HDTVI (see Figure 1 C) therefore n represented the number of tumors analyzed from at least 3 mice per group (Figure 1D, 2B, 2D, 2F, 2G).

RNA sequencing

RNA sequencing was done with the help of the "Transcriptome and Genome Analysis Laboratory (TAL), University of Göttingen, Germany. RNA was extracted via Trizol extraction protocol. Quality control was done by Agilent Bioanalyzer 2100. As starting material for the library preparation, 0.5µg of total RNA was used. The libraries were generated according to the TruSeq mRNA Sample Preparation Kits v2 Kit from Illumina (Cat. N°RS−122-2002). The fluorometric based QuantiFluor™ dsDNA System from Promega (Mannheim, Germany) was used for accurate quantitation of cDNA libraries. The size of final cDNA libraries was determined by using the Fragment Analyzer from Advanced Bioanalytical. cDNA libraries were amplified and sequenced by using the cBot and

HiSeq4000 from Illumina (SR; 1×50bp; ca. 30 Mio reads per sample). Sequence images were transformed to *bcl* files using Illumina software BaseCaller, which were demultiplexed to *fastq* files with *bcl2fastq* and quality checks were done via *fastqc*. Sequences were aligned to the genome reference (mm9) using the STAR alignment software (version 2.3.0e) allowing for 2 mismatches within 50 bases. Subsequently, filtering of unique hits and counting were conducted with SAMtools (version 0.1.18) and HTSeq (version 0.6.1p1). Read counts were analyzed in the R/Bioconductor environment (version 3.2, www.bioconductor.org) using the DESeq2 package (version 1.8.1). Candidate genes were filtered to a minimum of 2-fold change and FDR-corrected p-value < 0.05. Gene ontology enrichment analysis: the gene ontology analysis was carried out by using DAVID/EASE 6.7 [11].

Quantitative PCR

RNA isolation was performed using RNeasy Mini Kit (Qiagen) according to the manufacturers' instructions. For the RNA isolation from tumors the tumor pieces were shock frozen after harvest. The concentration and purity of RNA was determined and 1 µg RNA was used for cDNA synthesis using Superscript II reverse transcriptase kit (Invitrogen). First, 1 µg RNA, 2.5 µM OligodT and 0.5mM dNTP-mix were incubated at 65°C for 5 minutes for denaturation. The mixture was cooled down on ice for 2 minutes and mixed with 1X reaction buffer, 5 mM DTT, 0.5 U RNaseOUT (Invitrogen) and 10 U Superscript II reverse transcriptase and incubated 60 minutes at 50°C. For quantitative PCR analysis a reaction was performed with SYBR-Green MasterMix (Roche) on a StepOnePlus Real Time PCR system (Applied Biosystems). Expression levels were normalized based on the levels of the housekeeping gene cyclophilin. In the following table are the primer used for the real time PCR.

Gene	**forward-primer**	**reverse-primer**
Ccl2	GAA GGA ATG GGT CCA GAC AT	ACG GGT CAA CTT CAC ATT CA
Ccl4	GCC CTC TCT CTC CTC TTG CT	GTC TGC CTC TTT TGG TCA GG
Ccl5	TGC CCA CGT CAA GGA GTA TTT	TTC TCT GGG TTG GCA CAC A
Cxcl1	ACT GCA CCC AAA CCG AAG TC	TGG GGA CAC CTT TTA GCA TCT T
Cxcl2	CTC TCA AGG GCG GTC AAA AAG TT	TCA GAC AGC GAG GCA CAT CAG GTA
Cxcl10	GAC GGT CCG CTG CAA CTG	CTT CCC TAT GGC CCT CAT TCT
Cxcl13	CAT CAT GAG GTG GTG CAA AG	GGG TCA CAG TGC AAA GGA AT
Il1b	GTG GCT GTG GAG AAG CTG TG	GAA GGT CCA CGG GAA AGA CAC
Il6	ATG GTA CTC CAG AAG ACC AGA GGA	GTA TGA ACA ACG ATG ATG CAC TTG
Tnfa	GCC TAT GTC TCA GCC TCT TCT	AAC TGA TGA GAG GGA GGC CAT T

Flow cytometry

For flow cytometry analysis of the primary and subcutenous HCC immune infiltrates, livers were collected minced and digested twice with 1mg/ml of Collagenase IV (Sigma) for a total of 1h. For analysis of immune cells in organoids tumors, digestion was performed with BD Tissue Dissociation Reagent (661563) for 30min at 37C. The remaining organ pieces were

mashed and cell suspensions were filtered through a 70µm cell strainer. Digestion was stopped by addition of EDTA. Immune cells were enriched thanks to a 30%/40%/75% Percoll gradient with a 1700rpm 17min centrifugation. Tumor immune filtrates were then washed and stained for 15 to 20 min on ice, after a pre-stain of 5 min with α-CD16/CD32 (14-0161-82; eBioscience), with Fixable Viability Dye-eF780 (65-0865-18; eBioscience), α-CD45-FITC (11-0451-85; eBioscience), α-MHCII-PercP-Cy5.5 (107626, Biolegend), α-CD80-APC (104714; Biolegend), α-CD11b-BV650 (56340; BD), α-CD11c-BV785 (563735; BD), α-Ly6G-BV605 (563005; BD), α-Ly6C-AF700 (128024; Biolegend), α-F4/80-PE (12-4801-82, eBioscience), or with Fixable Viability Dye-eF780 (65-0865-18; ebioscience), α-CD45-BV786 (564225; BD), α-CD4-BuV496 (564667; BD) or α-CD4-AF700 (100429; Biolegend), α-CD8-BV605 (100744; Biolegend), α-CD69-FITC (557392; BD), α-PD1-APC (17-9985-82; eBioscience), α-TIM-3-PECy7 (119715; Biolegend), α-CTLA4-PerCP-Cy5.5 (106315; Biolegend) and α-Lag3-BV421 (125221, Biolegend).

For cytokines expression, immune cells were stimulated *ex vivo* with 20ng/ml PMA and 1µg/ml Ionomycin for 3h in RPMI, 10% FBS, 1x Non-Essential Amino Acid, 1mM Sodium Pyruvate, 10mM Hepes, 50µM β-Mercaptoethanol, 100 U/ml penicillin, and 100 µg/ml streptomycin and 2mM Glutamax containing Brefeldin A (Biolegend) then stain as previously described with α-CD16/CD32 (14-0161-82; eBioscience)Fixable Viability Dye-eF780 (65-0865-18; eBioscience), α-CD8 PeCy7 (Biolegend; 100722) and α-CD4-eFluor450 (65-0865-18; eBioscience, 48-0042-82). After 20min fixation in fixation/permeabilization solution (Cytofix/Cytoperm BD) and cells were stained overnight with α-IFNγ-PerCP-Cy5.5 (45-7311-82; eBioscience) in Perm/Wash buffer (BD). Samples were then fixed with 1% PFA and acquired on a Fortessa (BD) or Aurora (Cytek) and analyzed with FlowJo. For best

visualization of positive and negative fractions all gates were performed on dot plots rather than histograms. Cell doublets were excluded through FSC-A and SCC-A vs H dot plots and then debris were excluded by size exclusion with FSC-A vs SCC-A dot plots. Then, immune cells were gated as $CD45^+$, $Dead^-$. All the subsequent cells described below are therefore $Doublet^-$ (in FSC & SSC), $Debris^-$, $Dead^-$, $CD45^+$. Exhaustion, activation markers and cytokines were quantified as percentage of positive cells on gated $CD8^+$ cells. DCs were $CD11c^+$ $MHCII^{hi}$. The identification of MSDC by surface markers is still ill define [12]. A clear consensus was found on the expression of CD11b, Ly6C and Ly6G for the MDSCs while TAM were defined as $F4/80^{hi}$ with low to negative expression of Ly6C/G. Expression of Ly6C/G and F4/80 isn't mutually exclusive (data not shown). Our gating strategy was set-up to unsure that the Ly6C/G, F4/80 DP cells weren't counted twice e.g. as MDSC and as TAM. Those cells were considered as MDSC with our flow gating strategy. First cells were gated as $CD11b^+$ $CD11c^-$ and then M-MDSC were gated as $Ly6C^{hi}$, $Ly6G^{lo}$ and PMN-MDSC as $Ly6C^{int}$, $Ly6G^{hi}$. Then the M-MDSC and PMN-MDSC negative fraction of $CD11b^+$ $CD11c^-$ cells were gated for $F4/80^+$ to identified TAM.

Immunosuppressive assay.

Immune infiltrates from liver of tumor bearing mice were isolated as described in the flow cytometry method, stained with Fixable Viability Dye-eF780 (65-0865-18; ebioscience), α-CD45 FITC (11-0451-85; eBioscience), α-Ly6G-PeCy7 (25-5931-81; eBioscience) and α-Ly6C-AF700 (128024; Biolegend) and sorted by flow cytometry as $CD45^+$ $Ly6G^{hi}$ $Ly6C^{lo}$ for PMN-MDSCs and as $CD45^+$ $Ly6G^{lo}$, $Ly6C^{hi}$ for M-MDSCs. T cell were isolated from spleen of unchallenged WT mice by negative magnetic selection with MoJoSort kit (Biolegend; 480024) according to manufacturer's instructions with magnetic columns (Miltenyi) and then

stained with 5μM CelltraceViolet (Thermofischer; C34571) for 10min. T cells +/- MDSCs were stimulated for 3 days with 1ug/ml of plate-bound α-CD3 and α-CD28 at a ratio of 4/1. Then cells were stained for CD4 and CD8. CD8 T cell were then gate as described above as $Doublet^-$ (in FSC & SSC), $Debris^-$, $Dead^-$, CTV^- $CD8^+$. Proliferative, e.g., divided CD8 T cells were determined according to Celltrace $violet^{lo}$ staining intensity as shown in supplemental figure 3B. The immunosuppressive effect of the MDSC was quantified as the ratio of the percentages of proliferative T cells incubated with MDSC to of the percentages of proliferative T cells without any MDSC.

ELISA

The HMGB1 (IBL International) and Cxcl10 (R&D) ELISAs were performed according to the manufacturers' instructions using supernatants of cultured primary hepatocytes for 4 hours. The color reactions were detected spectrophotometrically using a plate reader at 450 nm with a correction at 540nm.

Statistical analysis

Statistical parameters including the minimal value of n per experiment, dispersion and precision measures (mean ± SEM) and statistical significance and the tests used are reported in the figures and figure legends. GraphPad PRISM software was used for statistical analysis. Samples with obvious technical or biological issue as well as prism-identified outliers were excluded from the analysis. Data were judged to be statistically significant based on t-test when comparing two samples, based on one-way ANOVA when comparing multiple samples with Dunnett's multiple or Šídák's multiple comparison test of the relevant groups which are indicated on the graphs. Unpaired tests were used unless the data were generated from

multiple independent experiments with known experimental bias, where a paired test was performed as for figures 2H, 3B, 3C, supplemental 2A and 3A. Log-rank (Mantel-Cox) test was performed for statistical analysis of the survivals. The p values were represented in the figures and indicated in the legends as n.s., not significant, * $p < 0.05$, ** $p < 0.01$, *** $p < 0.001$, **** $p < 0.0001$.

Supplemental References

1 Seiler A, Schneider M, Förster H, Roth S, Wirth EK, Culmsee C*, et al.* Glutathione peroxidase 4 senses and translates oxidative stress into 12/15-lipoxygenase dependent- and AIF-mediated cell death. Cell Metab 2008;**8**:237-48.
2 Newton K, Sun X, Dixit VM. Kinase RIP3 is dispensable for normal NF-kappa Bs, signaling by the B-cell and T-cell receptors, tumor necrosis factor receptor 1, and Toll-like receptors 2 and 4. Mol Cell Biol 2004;**24**:1464-9.
3 Sun D, Funk CD. Disruption of 12/15-lipoxygenase expression in peritoneal macrophages. Enhanced utilization of the 5-lipoxygenase pathway and diminished oxidation of low density lipoprotein. J Biol Chem 1996;**271**:24055-62.
4 Liliensiek B, Weigand MA, Bierhaus A, Nicklas W, Kasper M, Hofer S*, et al.* Receptor for advanced glycation end products (RAGE) regulates sepsis but not the adaptive immune response. J Clin Invest 2004;**113**:1641-50.
5 Godoy P, Hewitt NJ, Albrecht U, Andersen ME, Ansari N, Bhattacharya S*, et al.* Recent advances in 2D and 3D in vitro systems using primary hepatocytes, alternative hepatocyte sources and non-parenchymal liver cells and their use in investigating mechanisms of hepatotoxicity, cell signaling and ADME. Arch Toxicol 2013;**87**:1315-530.
6 Seehawer M, Heinzmann F, D'Artista L, Harbig J, Roux PF, Hoenicke L*, et al.* Author Correction: Necroptosis microenvironment directs lineage commitment in liver cancer. Nature 2018;**564**:E9.
7 Varga J, Nicolas A, Petrocelli V, Pesic M, Mahmoud A, Michels BE*, et al.* AKT-dependent NOTCH3 activation drives tumor progression in a model of mesenchymal colorectal cancer. J Exp Med 2020;**217**.
8 Fellmann C, Hoffmann T, Sridhar V, Hopfgartner B, Muhar M, Roth M*, et al.* An optimized microRNA backbone for effective single-copy RNAi. Cell Rep 2013;**5**:1704-13.
9 Carlson CM, Frandsen JL, Kirchhof N, McIvor RS, Largaespada DA. Somatic integration of an oncogene-harboring Sleeping Beauty transposon models liver tumor development in the mouse. Proc Natl Acad Sci U S A 2005;**102**:17059-64.
10 Soares KC, Foley K, Olino K, Leubner A, Mayo SC, Jain A*, et al.* A preclinical murine model of hepatic metastases. J Vis Exp 2014:51677.
11 Huang da W, Sherman BT, Lempicki RA. Systematic and integrative analysis of large gene lists using DAVID bioinformatics resources. Nat Protoc 2009;**4**:44-57.

12 Bronte V, Brandau S, Chen SH, Colombo MP, Frey AB, Greten TF*, et al.* Recommendations for myeloid-derived suppressor cell nomenclature and characterization standards. Nat Commun 2016;**7**:12150.